Monte Carlo simulations of microdosimetry and radiolytic species production at long time post proton irradiation using GATE and Geant4-DNA

Giovanna Rosa Fois, Hoang Ngoc Tran, Vincent Fiegel, Guillaume Blain, Sophie Chiavassa, Emeline Craff, Grégory Delpon, Manon Evin, Ferid Haddad, Sébastien Incerti, et al.

Monte Carlo simulations of microdosimetry and radiolytic species production at long time post proton irradiation using GATE and Geant4-DNA.

Giovanna Rosa Fois[1], Hoang Ngoc Tran[2], Vincent Fiegel[3], Guillaume Blain[4], Sophie Chiavassa[5], Emeline Craff[3], Grégory Delpon[5], Manon Evin[4], Ferid Haddad[3,4], Sébastien Incerti[2], Charbel Koumeir[3], Vincent Métivier[4], Quentin Mouchard[4], Freddy Poirier[3], Vincent Potiron[5,6], Noël Servagent[4], Johan Vandenborre[4] and Lydia Maigne[1*]

[1] Université Clermont Auvergne, CNRS, LPCA, 63000 Clermont-Ferrand, France

[2] Univ. Bordeaux, CNRS, LP2I, UMR 5797, F-33170 Gradignan, France

[3] GIP ARRONAX, Saint-Herblain, France

[4] Laboratoire SUBATECH, UMR 6457, CNRS/IN2P3, IMT Atlantique, Université de Nantes, France

[5] Institut de Cancérologie de l'Ouest, Saint-Herblain, France

[6] US2B, Nantes Université, CNRS, UMR 6286, France

*Corresponding author: lydia.maigne@clermont.in2p3.fr

ABSTRACT

Purpose: The radiobiological effectiveness of radiation in cancer treatment can be studied at different scales (molecular to organ scale) and at different times post-irradiation. The production of free radicals and reactive oxygen species during water radiolysis is particularly relevant to understanding the fundamental mechanisms playing a role in observed biological outcomes. The development of Monte Carlo tools integrating the simulation of physical, physico-chemical, and chemical stages after radiation should be validated with experimental data. Therefore, in this study, we propose to validate Geant4-DNA chemistry through the simulation of water radiolysis and Fricke dosimetry experiments on a proton preclinical beam line.

Material and methods: In this study, we used the GATE Monte Carlo simulation platform (version 9.3) to simulate a 67.5 MeV proton beam produced with the ARRONAX isochronous cyclotron (IBA Cyclone 70XP) at conventional dose rate (0.2 Gy/s) to simulate the irradiation of ultra-pure liquid water samples and Fricke dosimeter. We compared the depth dose profile with measurements performed with a plane parallel Advanced PTW 34045 Markus ionization chamber. Then, a new Geant4-DNA chemistry application proposed from Geant4 version 11.2 has been used to assess the evolution of $HO^{\bullet}$, e^{-}_{aq}, H_3O^{+}, H_2O_2, H_2, $HO_2^{\bullet}$, HO_2^{-}, $O_2^{\bullet-}$ and HO^{-} reactive species along time until one-hour post-irradiation. In particular, the effect of oxygen and pH has been investigated through comparisons with experimental measurements of radiolytic yields for H_2O_2 and Fe^{3+}.

Results: GATE simulations reproduced, within 4%, the depth dose profile in liquid water. With Geant4-DNA, we were able to reproduce experimental H_2O_2 radiolytic yields one-hour post-irradiation in aerated and deaerated conditions, showing the impact of small changes in oxygen concentrations on species evolution along time. For the Fricke dosimeter, simulated $G(Fe^{3+})$ is 15.97 ± 0.02 molecules/100 eV which is 11% higher than the measured value (14.4 ± 0.4 molecules/100 eV).

Conclusions: These results aim to be consolidated by new comparisons involving other radiolytic species, such as e^{-}_{aq} or , $O_2^{\bullet-}$ to further study the mechanisms underlying the FLASH effect observed at ultra-high dose rates (UHDR).

Keywords: Monte Carlo, GATE, Geant4-DNA, microdosimetry, water radiolysis

1. INTRODUCTION

In recent years, many preclinical beams have been set up to study the radiobiological effect of radiation at different scales, from cells to small animals. The radiobiological effectiveness depends on various parameters: the radiation quality of the beam, the dose, the dose rate, and the fractionation used. It has been shown that changes in cell sensitivity, cell repair capacities, repopulation, oxygenation, and modifications to the cell microenvironment can play a significant role[1,2]. The production of free radicals through water radiolysis represents a major part of radiation effect on biological matter[3]. Comprehension of radiolysis mechanisms along irradiation would definitively help understand biological outcomes observed.

Monte Carlo Track Structure codes have an important role to play in predicting direct and indirect effects of radiation at molecular scale. To that purpose, the open source and open access Geant4-DNA code[4–8] has been extensively developed and validated to model physical (10^{-15} s), physico-chemical (10^{-15} to 10^{-12} s) and chemical stages (10^{-12} to 10^{-6} s) following irradiation[9–12]. With the Geant4-DNA chemistry module, reactions and diffusion of molecules during water radiolysis can be simulated using two methods: the step-by-step (SBS)[10] and the independent reaction time (IRT)[13,14]. Recently, the code has been developed to be able to follow the diffusion and chemical interactions of radiolytic species until minutes post-irradiation[15]. In the new version of the code, a compartment-based model is developed to simulate the distribution of species along time, from heterogeneous distribution (a few ns after irradiation) to homogeneous distribution (minutes after irradiation). By using the reaction-diffusion master equation (RDME), this mesoscopic model divides the simulation volume into sufficiently small sub-volumes (so-called voxels) where species are assumed homogeneously mixed and can react between each other. Reactions between molecules take place within the voxels, while species can move from one voxel to an adjacent one by diffusion. The resolution of the system can change along time with voxels increasing in size. However, at the beginning of water radiolysis (from a few ps to ns), since the spatial distribution of the chemical species is concentrated in very small volumes mimicking radiation-induced spurs along the track, the evolution of the chemical species is described by using the step-by-step (SBS) Brownian dynamics model. The SBS is used to simulate the detailed trajectories of the individual species until 5 ns post-irradiation, and then the RDME method is applied. The combination between SBS and RDME methods is called SBS-RDME model. Further, a scavenger model has been implemented in the SBS method of Geant4-DNA to be able to simulate the presence of scavengers in water radiolysis experiments[16].

In this study, we used the Geant4-DNA Monte Carlo Track structure code (MCTS) available in version 11.2 of Geant4 with the SBS-RDME method proposed by Tran et al.[15] and Chappuis et al.[16] to simulate water radiolysis experiments for 67.5 MeV protons produced with the ARRONAX isochronous cyclotron (IBA Cyclone 70XP) at conventional dose rate (0.2 Gy/s). We first describe the beamline setup that has been simulated with the GATE platform[17–20] to irradiate a volume of 1.4 mL of pure water to reproduce the exact experimental conditions of Blain et al.[21]. Then, we provide a method to assess information about physics processes occurring in a cubic micrometric target localized at the center of the irradiated volume, and about $HO^{\bullet}$, e_{aq}^{-}, H_3O^{+}, H_2O_2, H_2, $HO_2^{\bullet}$, HO_2^{-}, $O_2^{\bullet-}$ and HO^{-} species evolution along time (from 10^{-12} s to 1 hour) in aerated and deaerated conditions. We also conducted experiments and simulations using a Fricke dosimeter.

2. MATERIAL AND METHODS

2.A. Description of the ARRONAX cyclotron dose delivery

ARRONAX is an isochronous cyclotron (IBA Cyclone 70XP) producing protons (30 MeV to 70 MeV), deuterons (15 MeV to 35 MeV), and alpha particles (67.5 MeV). Using a dedicated pulsing device[22] at various beam intensities (from 1 pA to 20 µA), the cyclotron can provide proton beams with a range of dose rates varying from 0.2 Gy/s (conventional dose rate) to 60 kGy/s (Very-High Dose Rate). The beam intensity was monitored in line by using an ionization chamber, which was calibrated to the signal of a Faraday cup at the sample position. All experiments were performed with a beam intensity of 40 pA at a dose-rate of 0.2 Gy/s.

2.B. Calculation of dose profiles

67.5 MeV proton beam line available at the ARRONAX isochronous cyclotron (IBA Cyclone 70XP) has been simulated using the GATE platform (version 9.3)[17–20] based on Geant4[23] version 11.2. The proton source, placed in a vacuum environment, had a Gaussian energy distribution of 67.5 MeV with 0.35 MeV FWHM. At the first collimator, it was elliptical with a FWHM of 2 and 3 mm in X and Y directions, respectively. The monodirectional beam was then obtained getting through a 50 µm thick Kapton exit window positioned at 0.01 mm from the source, a 51.7 µm tungsten foil diffuser at 50.06 mm from the source, and two aluminum collimators of 15 mm internal diameter positioned at 1.5 m and 1.7 m respectively from the source to spread and homogenize the beam before interacting with a water volume (1.4 mL filled with the G4_WATER material) at 1.84 m from the source (Figure 1). The range thresholds (cuts) for secondary particles have been fixed to 10 mm in all geometries and 0.1

µm in the water target volume. The QGSP_BIC_EMZ physics list has been selected with a limitation on the step size to 1 mm in all geometries and 100 µm in the target volume. The number of simulated protons was fixed to 10^7 to keep a statistical uncertainty below 2%. The simulated depth dose profile was then calculated using a DoseActor (GATE tool allowing the recording of energy deposited in a voxel volume) attached to the target volume with a 5×5×0.1 mm resolution respectively in X, Y, and Z directions to integrate the dose in the XY plane. The Pristine Bragg Peak was also measured in a 15×10×40 cm^3 water phantom using a parallel plane Advanced PTW 34045 Markus ionization chamber according to the International Atomic Energy Agency Technical Report Series (IAEA TRS) 398 Code of Practice[24]. Measurements were performed every millimeter until 30 mm depth and every 0.5 mm after. The measured dose fluctuations were estimated within 1%. Range estimations were conventionally calculated as the position of the 80% level of the distal fall-off.

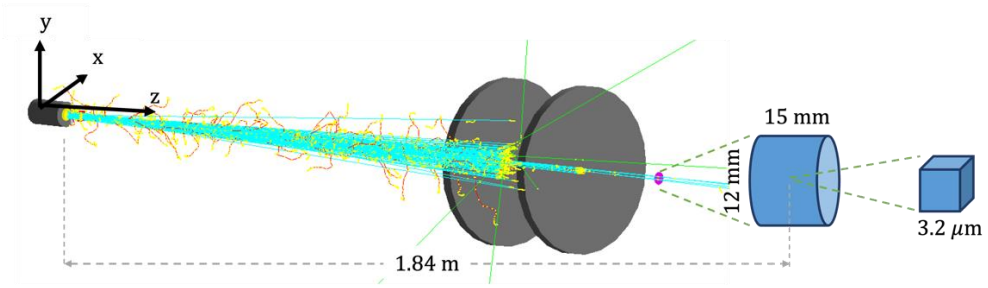

Figure 1 - GATE simulation of the beamline setup.

2.C. Calculation of microdosimetry spectra

To reproduce the irradiation conditions encountered during water radiolysis experiments, we used the beam described in section 2.A. using 1.64×10^{10} primary protons. The target volume was a cylindrical water phantom (diameter: 12 mm, height: 15 mm), irradiated from the bottom surface and centered at 1.84 m from the source in the plateau region ensuring a mean linear energy transfer (LET) of 1.20 keV.µm^{-1} and LET variations below 5% along particle tracks. A phase space (PhSp) file collecting information about 166 particles (146 protons and 21 delta-rays produced outside the volume) entering a 3.2 µm side cubic volume placed at the center of the cylindrical volume was collected. Phase space analysis for protons shows a Gaussian energy distribution with a mean value of 59.41 MeV and a full width at half maximum (FWHM) of 0.95 MeV, such protons were then considered as source particles for microdosimetry study. Using GATE with the Geant4-DNA (Geant4 version 11.2) physics lists options 2, 4, and 6, we first evaluated the percentage contribution of every physical process for every Geant4-DNA option. While option 2 is an accelerated version of the default Geant4-DNA

physics list, simulating electron interactions up to 1 MeV; in option 4, alternative models[25–27] for electron elastic scattering, ionization and excitation are included at low energy (10 eV – 10 keV) but vibration and attachment processes are not considered. In option 6, the implementation of the interaction cross sections of the CPA100 track structure code[28] is available for electrons (applicable between 11 eV and 255 keV).

Using protons with 59.41 MeV energy, we evaluated the total energy spectrum using the Geant4-DNA physics list option 2. The electrons leaving the 3.2 µm side target volume were ignored. We highlighted the contribution of dominant processes for protons and electrons to the total energy spectrum.

2.D. Calculation of radiolytic species production

Time-dependent radiolytic G values are calculated from 10^{-12} s until one hour after irradiation for the $HO^{\bullet}$, e_{aq}^{-}, H_3O^{+}, H_2O_2, H_2, $HO_2^{\bullet}$, HO_2^{-}, $O_2^{\bullet-}$ and HO^{-} radiolytic species in the 3.2 µm side liquid water box using Geant4-DNA physics list option 2. We used a new Geant4-DNA example, named UHDR (examples/extended/medical/dna/UHDR), available from Geant4.11.2 version to activate the SBS-RDME model, as described in Tran et al.[15]. In this model, the chemical stage is simulated through three sub-stages: the microscopic stage where the SBS method is used to follow the exact position of species produced in discrete time steps, then, at time t_1= 5 ns starts the mesoscopic stage where a uniform 3D Cartesian mesh of 512^3 voxels (corresponding to an initial voxel size of 6.25 nm) is created for the compartment-based model, to evolve to a single voxel when the homogeneous sub-stage starts describing the time-evolution probability of the chemical species until the end of the simulation.

The Geant4-DNA SBS model uses by default an approach called “dynamic time step”[10].

In this approach, time steps are chosen as a function of the distance between reactants. Depending on this distance, a probability of diffusion without any reactions is converted into a diffusion time where species is considered free to diffuse. However, the dynamic time step approach may lead to numerous small-time steps. To avoid this scenario, the Minimum Time Step technique and the Brownian Bridge technique have been added to limit the number of time steps. While Minimum Time Step limits the minimum time step allowed for each pair of reactants, the Brownian Bridge technique computes the probability of encounter during their Minimum Time Step and compensates for “missed” reactions. The Minimum Time Step is set to 1 ps in this work. During mesoscopic stage, the hRDME[29] approach is used to adapt the size of the voxels from the mesh of 512^3 voxels until there is only one voxel covering the

whole simulation volume. Note that in these simulations, molecules diffuse and react in the bounded volume (that is, limited by geometrical boundaries). These conditions enabled to confine the chemical molecules in the considered volume by bouncing them off the walls of the volume.

A parameter named "cutoff dose" allows to set the number of particles reaching the target volume at the same time. In this study, we considered a low cutoff value of 0.01 Gy. Primary protons (part of a run) are generated until the total energy deposited in the volume results in a dose of at least 0.01 Gy (corresponding to the cutoff value). For this low cutoff value, one or two protons are enough to reach this dose threshold. Protons in the same run are not independent, they come at the same time and, once the energy deposition ends, the chemistry is activated for all incident protons. Note that the secondary electrons leaving the 3.2 µm side target volume will be ignored.

Since the homogeneous stage can extend the simulation to a long-time post proton irradiation (a few minutes), the presence of oxygen and pH acid-base equilibrium in the medium is crucial to chemical species evolution. Geant4-DNA simulates the presence of oxygen and pH acid-base equilibrium in scavenger models for both SBS and IRT models. In these models, scavengers are treated as a continuum that is homogeneously distributed in water. In this work, this effect is incorporated during the chemical stage by specifying scavenger chemical reactions and scavenger concentrations[16]. The pH is determined by the concentrations of acids and bases (scavengers) in the solution. The direct interaction between radiation and scavenger, which would normally occur in the physical stage of the Geant4-DNA simulation, is not considered. All equations corresponding to the simulated water radiolysis reactions are listed in the Appendix. The computation time, for less than 1% uncertainty, was about 10 hours on 100 CPUs (3.4 GHz, AMD EPYC 7542).

2.D.1. Aerated conditions

We compared simulated H_2O_2 G values obtained 1-hour post-irradiation with experimental measurements from Blain et al. [21] who measured track segment $G_{TS}(H_2O_2)$ radiolytic creation yields in the plateau region using the well-known Ghormley's tri-iodide protocol[30]; $[H_2O_2]$ was determined under 19% of oxygen for 5 doses from 20 to 80 Gy, and each dataset was replicated 2 or 3 times, as described in previous work[21]. Further, the simulated pH was fixed to 5.5 according to the ultra-pure water pH measured; this value is due to the CO_2 absorption in water during the purification process. Because all other ions have been removed, the ultra-pure water

pH becomes driven by the chemistry of the couple CO_2/HCO_3^- causing the pH level to drop to a value of 5.5. CO_2 concentration was 1.4 10^{-5} mol.L^{-1}. In simulation we neglected the reactions between the radiolytic species and CO_2/HCO_3^-. For pH 5.5, the concentration of HO^- and H_3O^+ were fixed to 3.16 10^{-9} and 3.16 10^{-6} mol.L^{-1} respectively. Further, we considered only oxygen, neglecting the effect of nitrogen and other compounds.

2.D.2. Deaerated conditions

The simulated G values for H_2O_2, one hour post-irradiation, obtained for different levels of O_2 (from a fully deoxygenated condition hypothesis equivalent to a 0% O_2 atmosphere to 3 %), were compared to experimental measurements from co-authors[21]. pH was fixed to 5.5 to reproduce the ultra-pure water used in experiments. Experimental deaerated conditions were obtained by degassing the water in a Duran flask for one hour, reaching 0.3% in O_2. Water was then transferred to the radiolysis cell achieving an O_2 concentration between 2 and 3%.

2.E. Fricke dosimeter

We simulated the evolution of ferric ion (Fe^{3+}) G value (molecule/100 eV) as a function of time and compared with experimental data performed with a Fricke dosimeter on the ARRONAX beam line. The super Fricke version of this chemical dosimeter was used, allowing increased dose rates studies. This dosimeter was prepared with 0.4 mol.L^{-1} H_2SO_4, 10^{-3} mol.L^{-1} NaCl and 10^{-2} mol.L^{-1} of Mohr salt (ammonium ferrous sulfate hexahydrate) as initial Fe^{2+} source. The concentrations of Fe^{3+} ions created from water radiolysis species were measured (with at least 3 replicates) by their absorbance at 304 nm one hour after proton irradiation for 32.9, 43.9, 55.1, 66.0, 77.4 and 88.6 Gy. The pH was measured using a pH-meter (PHM220 model, Radiometer SAS, Copenhagen, Denmark) and a pH probe (Crison Instruments™, Barcelona, Spain). The measured pH was 0.4 ± 0.1. For pH 0.4, the concentrations of HO^- and H_3O^+ where 2.51 10^{-14} and 0.398 mol.L^{-1} respectively.

For simulations, the concentration of ferrous ions (Fe^{2+}) was set to 10 mM, pH was fixed to 0.4 and oxygen concentration was 19 %. We complemented the code with the following specific reactions (equations 1, 2, 3, and 4)[31] and associated rate constants:

$$Fe^{2+} + HO^{\bullet} \rightarrow Fe^{3+} + HO^- \qquad k = 3.4\ 10^8\ L\ mol^{-1}s^{-1} \qquad (1)$$

$$Fe^{2+} + HO_2^{\bullet} \rightarrow Fe^{3+} + HO_2^- \qquad k = 7.9\ 10^5\ L\ mol^{-1}s^{-1} \qquad (2)$$

$$Fe^{2+} + H_2O_2 \rightarrow Fe^{3+} + HO^{\bullet} + HO^- \qquad k = 52\ \ L\ mol^{-1}s^{-1} \qquad (3)$$

$$Fe^{2+} + H^{\bullet} \rightarrow Fe^{3+} + H_2 \quad k = 1.3\ 10^7\ L\ mol^{-1}s^{-1} \tag{4}$$

Further, we tested the effect of the solution acidity on ionic strength modification. For that purpose, we performed simulations using corrected reaction rate constants (see Appendix), as proposed by Ramos-Méndez et al.[32].

Finally, to take into account the presence of H_2SO_4 we added 0.4 mol.L^{-1} of HSO_4^- in our simulation (concentration of SO_4^{2-} was 1.4 10^{-2} mol.L^{-1}) implementing the following reactions[33] (from 5 to 12) with their reaction rate constants corrected for ionic strength:

$$HO^{\bullet} + HSO_4^- \rightarrow H_2O + SO_4^{\bullet -} \quad k = 1.5\ 10^5\ L\ mol^{-1}s^{-1} \tag{5}$$

$$H + SO_4^{\bullet -} \rightarrow HSO_4^- \quad k = 1.0\ 10^{10}\ L\ mol^{-1}s^{-1} \tag{6}$$

$$H_2O_2 + SO_4^{\bullet -} \rightarrow HO_2^{\bullet} + HSO_4^- \quad k = 1.2\ 10^7\ L\ mol^{-1}s^{-1} \tag{7}$$

$$HO^- + SO_4^{\bullet -} \rightarrow HO^{\bullet} + SO_4^{2-} \quad k = 1.56\ 10^8\ (*)\ L\ mol^{-1}s^{-1} \tag{8}$$

$$SO_4^{\bullet -} + SO_4^{\bullet -} \rightarrow S_2O_8^{2-} \quad k = 8.28\ 10^8\ (*)\ L\ mol^{-1}s^{-1} \tag{9}$$

$$SO_4^{\bullet -} + Fe^{2+} \rightarrow Fe^{3+} + SO_4^{2-} \quad k = 2.79\ 10^8\ L\ mol^{-1}s^{-1} \tag{10}$$

$$e_{aq}^- + S_2O_8^{2-} \rightarrow SO_4^{\bullet -} + SO_4^{2-} \quad k = 4.25\ 10^{10}\ (*)\ L\ mol^{-1}s^{-1} \tag{11}$$

$$H^{\bullet} + S_2O_8^{2-} \rightarrow SO_4^{\bullet -} + HSO_4^- \quad k = 2.5\ 10^7\ L\ mol^{-1}s^{-1} \tag{12}$$

*Corrected reaction rate constant for ionic strength

We also studied the influence of small pH variation (from 0.3 to 1) on the G(Fe^{3+}) yield 1 hour post-irradiation. Further, to consolidate the consistent functioning of the code, we followed e_{aq}^- and $H^{\bullet}$ species along time responsible for $HO_2^{\bullet}$ species production (see equations 13 and 14) at early time post-irradiation.

$$e_{aq}^- + H^+ \rightarrow H^{\bullet} \quad k = 1.12\ 10^{10}\ L\ mol^{-1}s^{-1} \tag{13}$$

$$H^{\bullet} + O_2 \rightarrow HO_2^{\bullet} \quad k = 1.3\ 10^{10}\ L\ mol^{-1}s^{-1} \tag{14}$$

3. RESULTS

3.A. Depth-dose profile

Figure 2 shows the depth dose curve in G4_WATER (I=78 eV) obtained with GATE and measurements for the 67.5 MeV proton beam considering the same number of initial protons (experimentally measured using a Faraday cup). Statistical errors were too small to be

plotted in the figure. The point-to-point relative differences between the simulation and measurements were superimposed. Relative differences remain below 4% until 15 mm and 2% after this depth value. A range value of 34.79 mm was obtained for GATE and measurements.

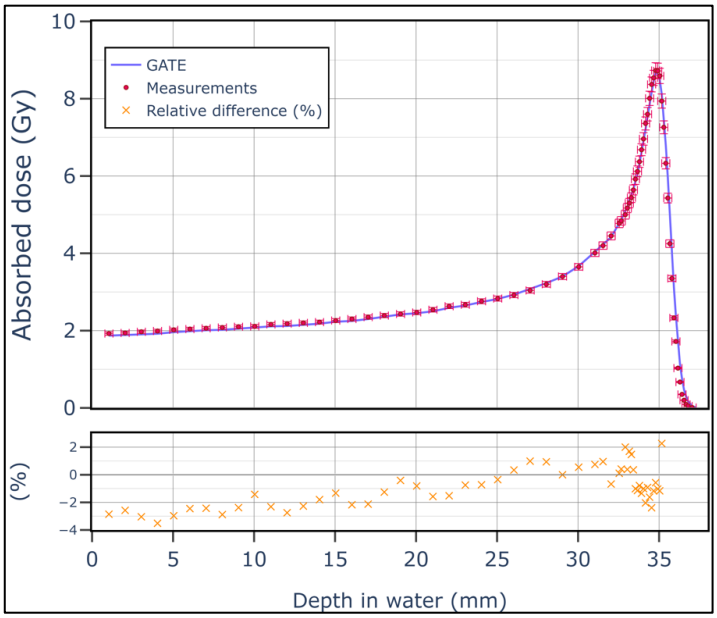

Figure 2 - Depth dose curves in water (I = 78 eV) obtained using GATE (blue curve) and measurements (red dots) for the ARRONAX 67.5 MeV proton beam line considering the same number of initial protons. Point-to-point relative dose differences (%) between measurements and simulations are plotted at the bottom.

3.B. Physical processes at the microscale

Figure 3 presents the percentage contribution of every physical process for Geant4-DNA options 2, 4, and 6, calculated in the 3.2 µm side cubic liquid water target with GATE using a 59.41 MeV (LET=1.20 keV.µm^{-1}) monoenergetic proton beam. Processes involved are ionization, excitation for both protons and electrons and vibration, solvation, and elastic scattering for secondary electron processes. The two dominant processes are electron and proton ionizations.

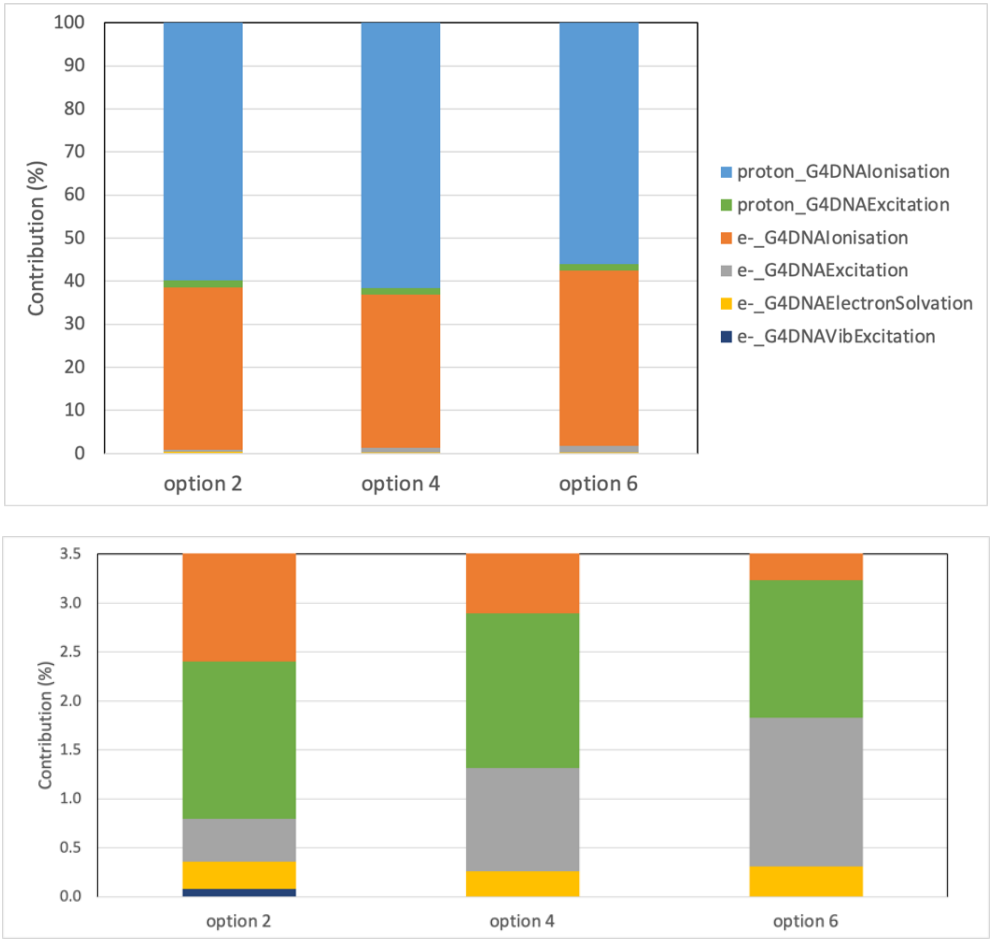

Figure 3 - Percentage contribution of every physical process to the energy deposition: proton ionization in blue, proton excitation in green, electron ionization in orange, electron excitation in grey, electron solvation in yellow, and electron vibration in dark blue. At the bottom, Contributions between 0 and 3.5% are highlighted.

In addition, in Figure 4, we present the energy spectrum obtained with Geant4-DNA option 2 and we emphasized the contributions of proton and electron ionization to the total energy spectrum. Other processes (electron and proton excitations as well as electron solvation) are contributing to energy depositions at very low energies (below 15 eV).

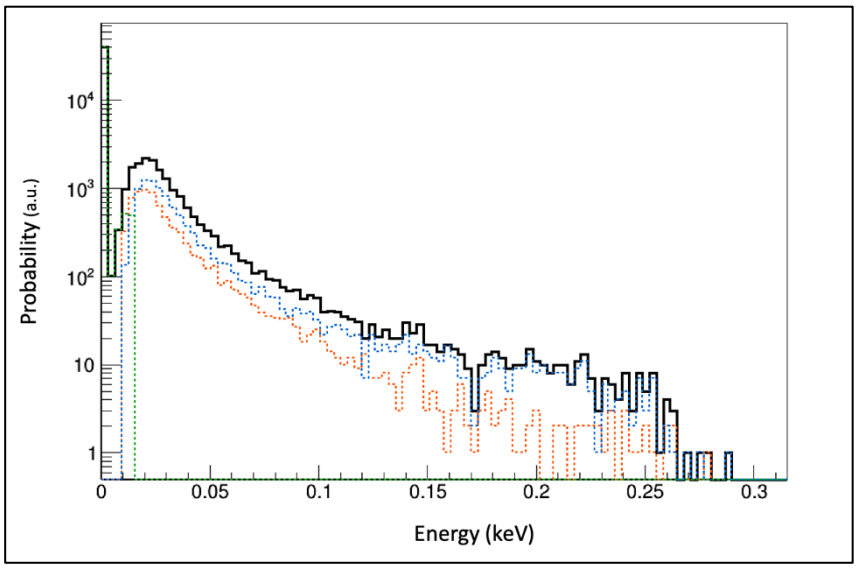

Figure 4 - Energy spectrum (black line) obtained with Geant4-DNA option 2. Contributions from proton (blue) and electron (red) ionization are shown. Contributions from all the other processes are responsible for the very low energy part of the plot (green).

3.C. Radiolytic species yields under conventional radiation

3.C.1 Aerated conditions

Figure 5 presents the simulated time-dependent yields (from 10^{-12} s to 1 hour) of different chemical species ($HO^{\bullet}$, e^-_{aq}, H_3O^+, H_2O_2, H_2, $HO_2^{\bullet}$, HO_2^-, $O_2^{\bullet-}$ and HO^-) obtained in a 3.2 µm side cubic liquid water volume (19% of oxygen) irradiated with a monoenergetic 59.41 MeV proton beam (LET=1.20 keV.µm^{-1}). The yield uncertainty values remain under 5%. At 60 min, G values for H_2O_2 and H_2 species are respectively 1.96 and 0.39 molecules/100 eV.

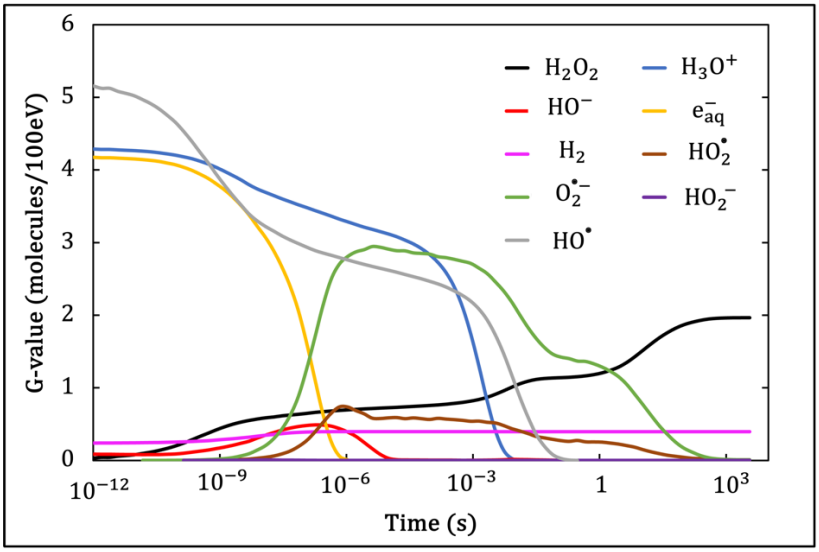

Figure 5 – Simulated time-dependent radical yields (G values) for water irradiations with 59.41 MeV proton beam in aerated conditions (19% of oxygen). $HO^{\bullet}$ (grey), e^-_{aq} (yellow), H_3O^+ (dark blue), H_2O_2 (black), H_2 (magenta), HO^- (red), $HO_2^{\bullet-}$ (purple), $HO_2^{\bullet}$ (brown), $O_2^{\bullet-}$ (green).

3.C.2 Deaerated conditions

In Figure 6 we present the simulated time-dependent yields (from 10^{-12} s to 60 min) for different chemical species ($HO^{\bullet}$, e_{aq}^{-}, H_3O^{+}, H_2O_2, H_2, $HO_2^{\bullet}$, HO_2^{-}, $O_2^{\bullet-}$ and HO^{-}) obtained in a 3.2 µm cubic liquid water irradiated with a monoenergetic 59.41 MeV proton beam (LET=1.20 keV.µm^{-1}). At 1 hour, G values for H_2O_2 and H_2 species are respectively 1.05 and 1.24 molecules/100 eV.

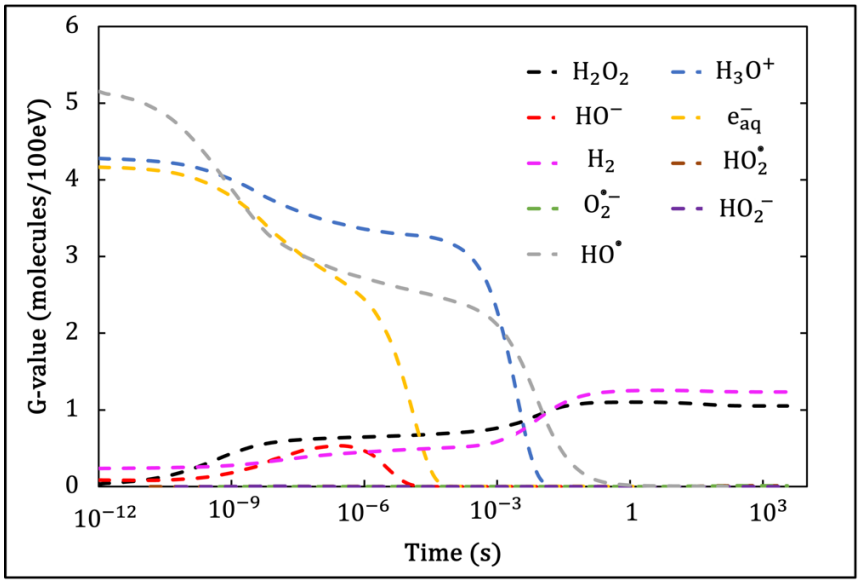

Figure 6 – Simulated time-dependent radical yields (G values) for water irradiations with 59.41 MeV proton beam in deaerated conditions (0% oxygen). $HO^{\bullet}$ (grey), e_{aq}^{-} (yellow), H_3O^{+} (dark blue), H_2O_2 (black), H_2 (magenta), HO^{-} (red), $HO_2^{\bullet-}$ (purple), $HO_2^{\bullet}$ (brown), $O_2^{\bullet-}$ (green).

In Figure 7 we summarize the evolution of H_2O_2, $HO_2^{\bullet}$, $O_2^{\bullet-}$, and e_{aq}^{-} species along time in aerated and deaerated conditions. After continually increasing along time, G value of H_2O_2 remains almost constant (1.05 ± 0.01 molecules/100 eV) from 50 ms until 1 hour in deaerated conditions. In aerated conditions (19% of oxygen), we can observe a final increase from 2 s to reach 1.96 ± 0.02 molecules/100 eV at 1 hour representing 46 % difference at this time. G(H_2O_2) values measured 1 hour post-irradiation are 1.98 ± 0.19 molecules/100 eV and 1.55 ± 0.20 molecules/100 eV for aerated and deaerated conditions respectively.

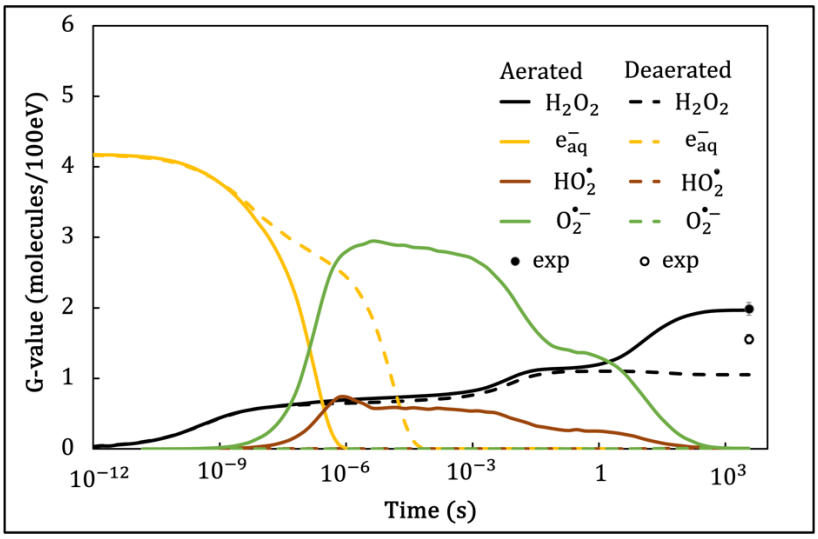

Figure 7 – Simulated time-dependent radical yields (G values) for water irradiations with 59.41 MeV proton beam in aerated (19% Oxygen - filled circles) and deaerated (0% Oxygen - open circles) conditions. H_2O_2 (black), e^-_{aq} (yellow), $HO^{\bullet}_2$ (brown), $O^{\bullet-}_2$ (green). G values for H_2O_2 are compared to experimental values (exp) measured 1-hour post-irradiation.

In Table 1 are summarized the simulated G(H_2O_2) values obtained 1 hour post-irradiation, while in Figure 8 we show the evolution of G(H_2O_2) along time for 3.10^{-4} % and 19 % of O_2. We understand that a minimal change in the oxygen level leads to important differences in G(H_2O_2) 1 hour post-irradiation. In Figure 8, we show that we can reproduce the experimental value of G(H_2O_2) obtained in deaerated conditions with an oxygen concentration of $3{\cdot}10^{-4}$ %.

O_2 concentration (%)	0	$3.0\ 10^{-4}$	2	3	19
O_2 concentration (mol.L^{-1})	0	$3.9\ 10^{-9}$	$2.6\ 10^{-5}$	$3.9\ 10^{-5}$	$2.5\ 10^{-4}$
G(H_2O_2) at 1 hour post-irradiation (molecules/100 eV)	1.05	1.53	1.89	1.92	1.96

Table 1 – Simulated G(H_2O_2) (molecules/100 eV) at 1 hour post-irradiation for different oxygen concentrations (% and mol.L^{-1}).

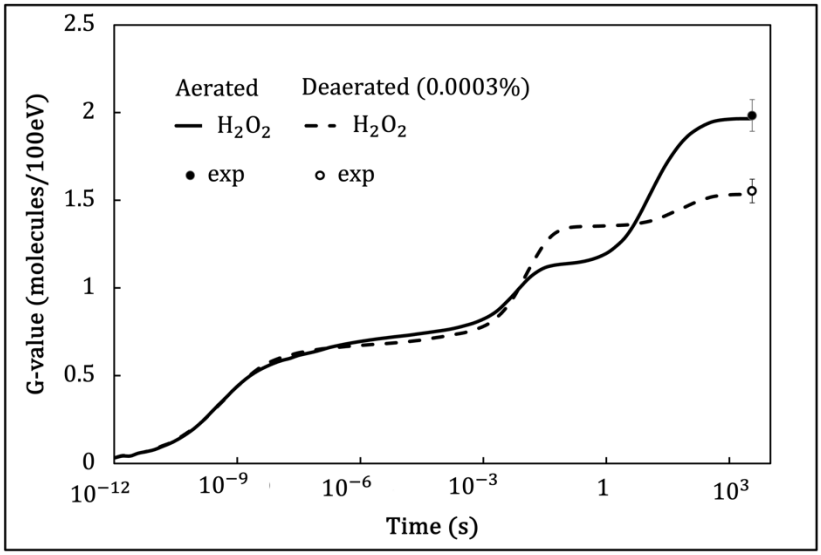

Figure 8 – Evolution of simulated time-dependent radical yields (G values) of H_2O_2 species along time for water irradiations with 59.41 MeV proton beam for 19 % and 3.10^{-4} % of O_2. Measured values obtained 1-hour post-irradiations in aerated and deaerated conditions are also presented.

3.D Fricke dosimeter

In Figure 9 we present the time evolution of G value of Fe^{3+} for 3 different simulation setups. First, we only considered the reactions for Fe^{2+} (equations 1 to 4). Second, we used corrected reaction rate constants for ionic strength (see Appendix). Third, we added reactions due to the presence of H_2SO_4 (equations 5 to 12). At one-hour post-irradiation, simulated $G(Fe^{3+})$ are 16.09 ± 0.03 molecules/100 eV (when only Fe^{2+} reactions are considered); 16.14 ± 0.03 molecules/100 eV (when correcting reaction rate constants for ionic strength); 15.97 ± 0.02 molecules/100 eV (when adding reaction involving HSO_4^-); while the measured yield is 14.4 ± 0.4 molecules/100 eV.

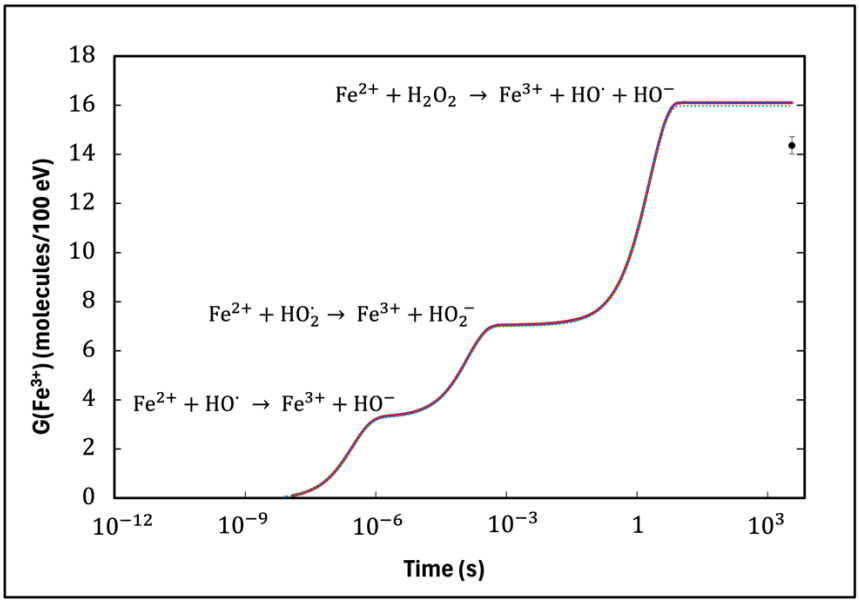

Figure 9 – Simulated time-dependent radical yields (G values) of Fe^{3+} from a 59.41 MeV proton beam irradiation of a Fricke solution for pH 0.4. The red curve is obtained with only Fe^{2+} reactions with $HO^{\bullet}$, $HO_2^{\bullet}$, H_2O_2 and $H^{\bullet}$. A blue dashed curve is obtained by modifying the reaction rate constants for ionic strength as proposed by Ramos-Mendez et al.[32]. A dashed green curve is obtained by adding H_2SO_4 scavenging reactions. Measurement is shown with a black dot (uncertainty 2.5%). The reactions between Fe^{2+} and $HO^{\bullet}$, $HO_2^{\bullet}$ and H_2O_2 are presented in the plot near the step when they contribute to the G value.

In Figure 10, we show the evolution of $G(Fe^{3+})$ as a function of pH. $G(Fe^{3+})$ yields decrease by 1.02 % between pH 0.3 and 1.

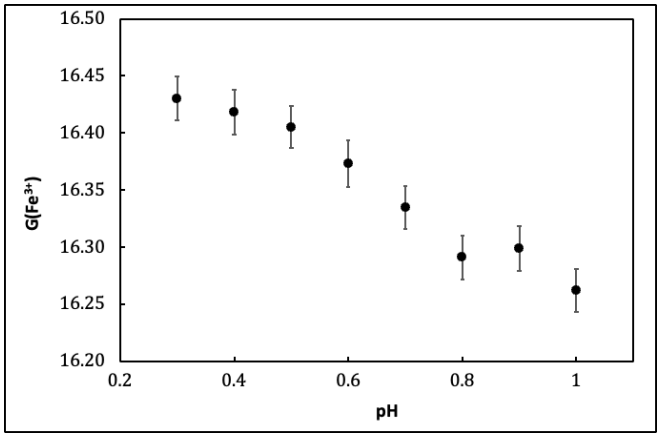

Figure 10 – Simulated time dependent radical yields (G values) of Fe^{3+} from a 59.41 MeV proton beam irradiation of a Fricke solution for pH values between 0.3 and 1 at one-hour post-irradiation.

In Figure 11, the evolution of $G(e_{aq}^-)$ and $G(H^{\cdot})$ values is plotted along time as a function of pH. The more pH is acid, the more e_{aq}^- species react faster with H^+ and the more $HO_2^{\cdot}$ species are produced to then foster the oxidation of Fe^{2+}.

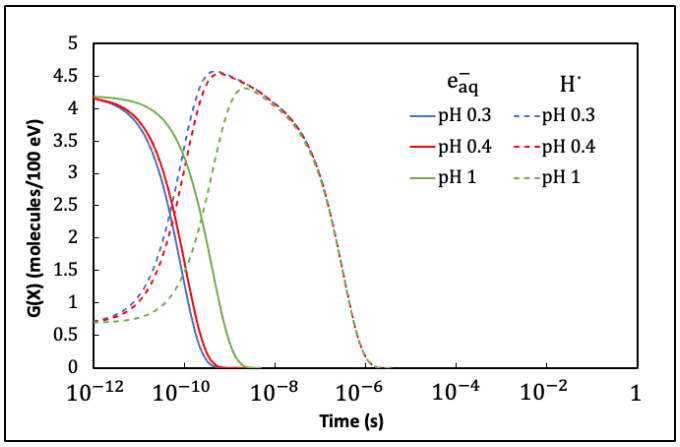

Figure 11 – Simulated time dependent radical yields (G values) of $H^{\cdot}$ and e^-_{aq} from a 59.41 MeV proton beam irradiation of a Fricke solution for pH 0.3 and pH 1 in aerated conditions.

4. DISCUSSION

4.1 Physical processes at the microscale

The contributions of physical processes obtained with the different Geant4-DNA physics lists are very comparable. As expected, proton and electron ionization processes are predominant with an energy contribution larger than 90 %. We can notice that the contribution of electron ionizations and excitations in Geant4-DNA option 6 are about 6% and 1% larger than in options 2 and 4. Option 2 is the only option simulating attachment and vibration processes while solvation, to reproduce the thermalization of electrons, is contributing equally whatever the option. From Figure 4, we notice that the maximum energy deposited in the 3.2 µm water cube is 300 eV with a maximum probability at 20 eV. Below 15 eV, electron and proton excitations as well as electron solvation are involved.

4.2 Radiolytic yields

The H_2O_2 production results from the competition of chemical reactions forming (equations 15 to 22 in Table 2) and consuming (equations 23 to 26 in Table 2) this species. While H_2O_2 is mainly formed by the recombination of hydroxyl radicals (equation 15), it can also be produced by chemical reactions involving dissolved oxygen (equations 16 to 19 in Table 2), especially in aerated conditions. To understand if the dissolved oxygen is impacting $G(H_2O_2)$ values at 1-hour post-irradiation, we plotted in the same figure (see Figure 7), H_2O_2, $HO_2^{\bullet}$, $O_2^{\bullet -}$ G values along time. We can notice that, in aerated conditions, while $G(HO^{\bullet})$ is not significantly impacted by the level of dissolved oxygen in solution (see Figure 5 and Figure 6),

e^-_{aq} species are depleted within 1 µs under oxygenated conditions, while they persist until 1 ms when the conditions are deaerated. Among the three main reactions involving hydrated electrons, equation 16 is not simulated in deaerated conditions explaining their slow consumption compared to aerated conditions. To emphasize the reactions involved in the production of H_2O_2 as a function of time (in aerated and deaerated conditions), we highlighted in Figure 12 the main reactions involved: from 1 ps to 7 s the main reaction is the recombination of hydroxyl radicals while after, the main reactions are involving HO_2^- species. In deaerated conditions, only reaction $HO^\bullet + HO^\bullet \longrightarrow H_2O_2$ is involved in H_2O_2 production, we observe that $G(H_2O_2)$ at 1-hour post-irradiation is increasing to 1.05 molecules/100 eV (46.6% decrease compared to the value in aerated conditions) explaining the ability for Geant4-DNA simulations to faithfully reproduce oxygen depletion by the pathway of ROS ($HO_2^-/O_2^{\bullet-}$) recombination through reactions (19-20).

Table 2 – Water radiolysis equations involving the formation and consumption of H_2O_2.

H_2O_2 formation reactions		H_2O_2 consumption reactions	
$HO^\bullet + HO^\bullet \longrightarrow H_2O_2$	(15)	$H_2O_2 + e^-_{aq} \longrightarrow HO^\bullet$	(23)
$e^-_{aq} + O_2 \longrightarrow O_2^{\bullet-}$	(16)	$H_2O_2 + H^\bullet \longrightarrow HO^\bullet + H_2O$	(24)
$H^\bullet + O_2 \longrightarrow HO_2^\bullet$	(17)	$H_2O_2 + HO^\bullet \longrightarrow HO_2^\bullet + H_2O$	(25)
$O_2^{\bullet-} + H^+ \leftrightharpoons HO_2^\bullet$	(18)	$H_2O_2 + HO^- \rightarrow HO_2^-$	(26)
$HO_2^\bullet + O_2^{\bullet-} \rightarrow HO_2^- + O_2$	(19)		
$HO_2^- + H_2O \rightarrow H_2O_2 + HO^-$	(20)		
$H_3O^+ + HO_2^- \rightarrow H_2O_2$	(21)		
$HO_2^\bullet + HO_2^\bullet \rightarrow H_2O_2 + O_2$	(22)		

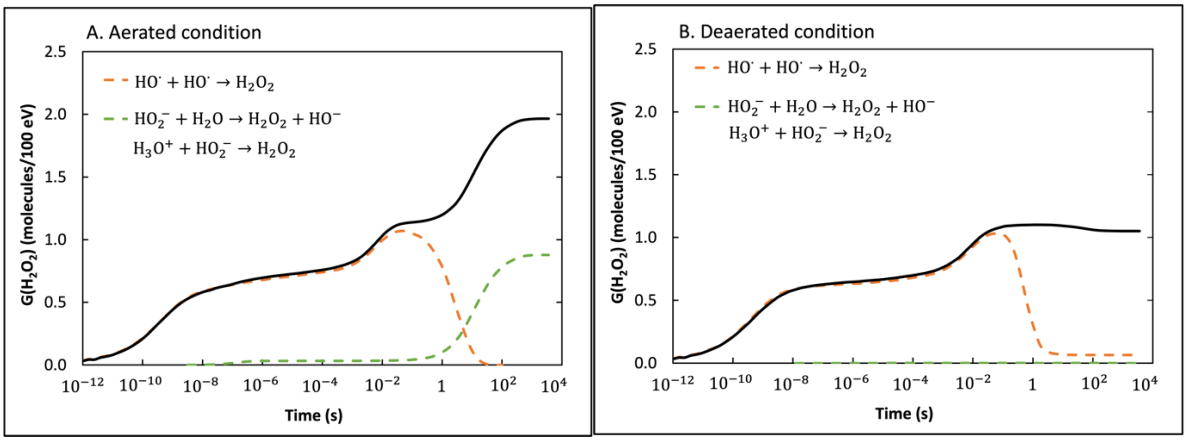

Figure 12 - Simulated $G(H_2O_2)$ values for water irradiations with 59.41 MeV proton beam are shown with black bold lines in aerated conditions (A) and deaerated conditions (B). Dashed curves are obtained only considering the production of H_2O_2 molecules through $HO^{\bullet} + HO^{\bullet}$ reaction (in orange) and only considering the production of H_2O_2 molecules through $HO_2^- + H_2O$ and $H_3O^+ + HO_2^-$ reactions (in green). In aerated conditions, the first part of the curve, from 0 to 7 s, involves a dominant chemical reaction: $HO^{\bullet} + HO^{\bullet} \longrightarrow H_2O_2$, the second part from 7 s to 1 hour involves two dominant reactions: $HO_2^- + H_2O \rightarrow H_2O_2 + OH^-$ and $H_3O^+ + HO_2^- \rightarrow H_2O_2$. In deaerated conditions, $G(H_2O_2)$ is dominated by the reaction $HO^{\bullet} + HO^{\bullet} \longrightarrow H_2O_2$.

4.3 Fricke dosimeter

In this study, we reproduced Fricke dosimetry by implementing chemical reactions involving the oxidation of ferrous ions (Fe^{2+}), corrected reaction rate constants for ionic strength, and reactions associated with the presence of sulfuric acid. Simulated $G(Fe^{3+})$ obtained 1-hour post-irradiation (15.97 ± 0.02 molecules/100 eV) is 11% higher than the experimental value (14.4 ± 0.4 molecules/100 eV). As shown in Figure 9, neither the consideration of ionic strength nor the implementation of reactions involving H_2SO_4 play a major role in the calculation of $G(Fe^{3+})$.

We tested the consistency of the code concerning the variation of pH following e_{aq}^- and $H^{\bullet}$. The code reproduces well the decrease of $G(Fe^{3+})$ as the pH increases.

When comparing to the literature, Pimblott and Laverne[34] show the effect of particle energy on $G(Fe^{3+})$ yield in IRT simulation for protons until one-second post-irradiation. For the same proton energy as used in this study, they obtain a $G(Fe^{3+})$ value of 14.45 molecules/100 eV. This value is 21.8% higher than our value (11.3 molecules/100 eV) obtained after one second, while our simulation shows an increase of $G(Fe^{3+})$ after one second and until one-minute post-irradiation to finally remains constant until one hour. However, the Pimblott and Laverne[34] $G(Fe^{3+})$ value remains very comparable with measurements.

Further, Audouin et al.[35] studied the chemistry of super-Fricke solutions along the Bragg peak curve for different 62 MeV proton beam intensities. In the low LET region, they obtained

an average G(Fe^{3+}) value of 14.9 ± 1.2 molecules/100 eV associated with an intensity range of 0.25 nA corresponding to a beam dose rate of 35 Gy/s. This value is 10 % lower than our simulated value but is very close to the measured value (3.3 % difference).

5. CONCLUSION

The reactive oxygen species (ROS) play a major role in the biological evolution of a cell system under irradiation (cell survival, cell death, cell signaling and inflammation-related factors). To compare the production of radiolytic species over a long-time post-irradiation, simulation tools must provide mechanisms for the diffusion of these species under the same conditions. In this paper, using Geant4-DNA version 11.2 implementing, in the UHDR example, a hybrid SBS method to follow diffusion and reactions of species until long-time post-irradiation, we reproduced water radiolysis experiments for different oxygen concentrations for a preclinical proton beam at conventional dose rates (0.2 Gy/s). At 1 hour post-irradiation, simulated G(H_2O_2) agrees within 2% with measured values. We also explored the ability of the Geant4-DNA toolkit to simulate Fricke dosimetry experiments. Simulated G(Fe^{3+}) differs by 11% from measurement. The simulations developed in this study will be provided to the user community through two new Geant4-DNA examples. This study aims to be complemented, in the near future, to understand the mechanisms underlying the FLASH effect occurring at ultra-high dose rates (UHDR), where higher concentration of radiolytic species within a short time interval may modify the chemical pathways. In particular, simulations of H_2O_2 yields will be compared with measurements proposed by Blain et al.[21] until 60 kGy/s.

6. ACKNOWLEDGEMENTS

This work was funded by Inserm Cancer PCSI “FLASHMOD” program and in part has been supported by grants from the French National Agency for Research “France 2030 investment plan” and ISITE NExT “Transformed” (ANR-16-IDEX-0007). We thank also the Geant4-DNA collaboration for their valuable support.

7. REFERENCES

1. Nickoloff JA, Taylor L, Sharma N, Kato TA. Exploiting DNA repair pathways for tumor sensitization, mitigation of resistance, and normal tissue protection in radiotherapy. *Cancer Drug Resist*. 2021;4(2):244. doi:10.20517/CDR.2020.89

2. Busato F, Khouzai B El, Mognato M. Biological Mechanisms to Reduce Radioresistance and Increase the Efficacy of Radiotherapy: State of the Art. *Int J Mol Sci*. 2022;23(18). doi:10.3390/IJMS231810211

3. Riley PA. Free Radicals in Biology: Oxidative Stress and the Effects of Ionizing Radiation. *https://doi.org/101080/09553009414550041*. 2009;65(1):27-33. doi:10.1080/09553009414550041

4. Tran HN, Chappuis F, Incerti S, Bochud F, Desorgher L. Geant4-DNA modeling of water radiolysis beyond the microsecond: an on-lattice stochastic approach. *Int J Mol Sci*. 2021;22:6023. doi:10.3390/ijms22116023

5. Bernal MA, Bordage MC, Brown JMC, et al. Track structure modeling in liquid water: A review of the Geant4-DNA very low energy extension of the Geant4 Monte Carlo simulation toolkit. *Phys Medica*. 2015;31(8):861-874. doi:10.1016/J.EJMP.2015.10.087

6. Incerti S, Ivanchenko A, Karamitros M, et al. Comparison of GEANT4 very low energy cross section models with experimental data in water. *Med Phys*. 2010;37(9):4692-4708. http://link.aip.org/link/MPHYA6/v37/i9/p4692/s1&Agg=doi

7. Incerti S, Baldacchino G, Bernal M, et al. The Geant4-DNA project. *Physics (College Park Md)*. 2009;01(02):1-27. http://arxiv.org/abs/0910.5684

8. Incerti S, Kyriakou I, Bernal MA, et al. Geant4-DNA example applications for track structure simulations in liquid water: A report from the Geant4-DNA Project. *Med Phys*. 2018;45(8):e722-e739. doi:10.1002/MP.13048

9. Karamitros M, MANTERO A, INCERTI S, et al. Modeling Radiation Chemistry in the Geant4 Toolkit. *Prog Nucl Sci Technol*. 2011;2(0). doi:10.15669/pnst.2.503

10. Karamitros M, Luan S, Bernal MA, et al. Diffusion-controlled reactions modeling in Geant4-DNA. *J Comput Phys*. 2014;274:841-882. doi:10.1016/J.JCP.2014.06.011

11. Baldacchino G, Bouffard S, Balanzat E, et al. Direct time-resolved measurement of

radical species formed in water by heavy ions irradiation. *Nucl Instruments Methods Phys Res Sect B Beam Interact with Mater Atoms*. 1998;146(1-4):528-532. doi:10.1016/S0168-583X(98)00463-7

12. Ramos-Méndez J, Shin WG, Karamitros M, et al. Independent reaction times method in Geant4-DNA: Implementation and performance. *Med Phys*. Published online 2020. doi:10.1002/mp.14490

13. Clifford P, Green NJB, Oldfield MJ, Pilling MJ, Pimblott SM. Stochastic models of multi-species kinetics in radiation-induced spurs. *J Chem Soc Faraday Trans 1 Phys Chem Condens Phases*. 1986;82(9):2673-2689. doi:10.1039/F19868202673

14. Plante I, Devroye L. Considerations for the independent reaction times and step-by-step methods for radiation chemistry simulations. *Radiat Phys Chem*. 2017;139:157-172. doi:10.1016/j.radphyschem.2017.03.021

15. Tran HN, Chappuis F, Incerti S, Bochud F, Desorgher L. Geant4-DNA Modeling of Water Radiolysis beyond the Microsecond: An On-Lattice Stochastic Approach. *Int J Mol Sci*. 2021;22(11). doi:10.3390/IJMS22116023

16. Chappuis F, Grilj V, Tran HN, et al. Modeling of scavenging systems in water radiolysis with Geant4-DNA. *Phys Med*. 2023;108:102549. doi:10.1016/j.ejmp.2023.102549

17. Jan S, Santin G, Strul D, et al. GATE: A simulation toolkit for PET and SPECT. *Phys Med Biol*. 2004;49(19):4543-4561. doi:10.1088/0031-9155/49/19/007

18. Sarrut D, Bardiès M, Boussion N, et al. A review of the use and potential of the GATE Monte Carlo simulation code for radiation therapy and dosimetry applications. *Med Phys*. 2014;41(6):064301. doi:10.1118/1.4871617

19. Jan S, Benoit D, Becheva E, et al. GATE V6: a major enhancement of the GATE simulation platform enabling modelling of CT and radiotherapy. *Phys Med Biol*. 2011;56(4):881-901.

20. Sarrut D, Arbor N, Baudier T, et al. The OpenGATE ecosystem for Monte Carlo simulation in medical physics. *Phys Med Biol*. 2022;67(18). doi:10.1088/1361-6560/ac8c83

21. Blain G, Vandenborre J, Villoing D, et al. Proton Irradiations at Ultra-High Dose Rate vs. Conventional Dose Rate: Strong Impact on Hydrogen Peroxide Yield.

https://doi.org/101667/RADE-22-000211. 2022;198(3):318-324. doi:10.1667/RADE-22-00021.1

22. Poirier F, Dr C, Goiziou X, et al. The pulsing chopper-based system of the ARRONAX C70XP cyclotron. In: *IPAC 2019 - 10th International Particle Accelerator Conference*. ; 2019:1948-1950. doi:10.18429/JACoW-IPAC2019-TUPTS008

23. Agostinelli S, Allison J, Amako K, et al. Geant4—a simulation toolkit. *Nucl Instrum Methods Phys Res A*. 2003;506(3):250-303. doi:10.1016/s0168-9002(03)01368-8

24. IAEA TRS 398. Absorbed Dose Determination in External Beam Radiotherapy. *At Energy*. Published online 2000:1-229. Accessed July 18, 2023. https://www.iaea.org/publications/5954/absorbed-dose-determination-in-external-beam-radiotherapy

25. Kyriakou I, Incerti S, Francis Z. Technical Note: Improvements in geant4 energy-loss model and the effect on low-energy electron transport in liquid water. *Med Phys*. 2015;42(7):3870-3876. doi:10.1118/1.4921613

26. I. Kyriakou, M. Sefl, V. Nourry SI. The impact of new Geant4-DNA cross section models on electron track structure simulations in liquid water. *J Appl Phys*. 2016;119(19). doi:10.1063/1.4950808

27. Kyriakou I, Emfietzoglou D, Ivanchenko V, et al. Microdosimetry of electrons in liquid water using the low-energy models of Geant4. *J Appl Phys*. 2017;122(2):024303. doi:10.1063/1.4992076

28. MC B, J B, S E, et al. Implementation of new physics models for low energy electrons in liquid water in Geant4-DNA. *Phys Med*. 2016;32(12):1833-1840. doi:10.1016/J.EJMP.2016.10.006

29. Hellander S, Hellander A. Hierarchical algorithm for the reaction-diffusion master equation. *J Chem Phys*. 2020;152(3):34104. doi:10.1063/1.5095075

30. Schwert GW, Neurath H, Kaufman S, et al. The yields of hydrogen and hydrogen' peroxide in the irradiation of oxygen saturated water with cobalt gamma-rays. *J Am Chem Soc*. 1954;76(12):3351-3352. doi:10.1021/JA01641A085

31. Plante I. Développement de codes de simulation Monte-Carlo de la radiolyse de l'eau par des électrons, ions lourds, photons et neutrons. Applications à divers sujets d'intérêt

expérimental. 2008;(2008). https://savoirs.usherbrooke.ca/bitstream/handle/11143/4292/Plante_Ianik_PhD_2008.pdf?sequence=3&isAllowed=y

32. Ramos-Méndez J, Domínguez-Kondo N, Schuemann J, McNamara A, Moreno-Barbosa E, Faddegon B. LET-dependent intertrack yields in proton irradiation at ultra-high dose rates relevant for FLASH therapy. *Radiat Res*. 2020;194(4):351-362. doi:10.1667/rade-20-00084.1

33. Autsavapromporn N, Meesungnoen J, Plante I, Jay-Gerin JP. Monte Carlo simulation study of the effects of acidity and LET on the primary free-radical and molecular yields of water radiolysis - Application to the Fricke dosimeter. *Can J Chem*. 2007;85(3):214-229. doi:10.1139/V07-021/ASSET/IMAGES/V07-021D.GIF

34. Pimblott SM, LaVerne JA. Effects of Track Structure on the Ion Radiolysis of the Fricke Dosimeter. *J Phys Chem A*. 2002;106(41):9420-9427. doi:10.1021/JP020830U

35. Audouin J, Paris C, Petter S, et al. Post-Bragg Peak keV-Secondary Electron Radiolysis Revealed by Track-Ends Imaging of High-Energy Protons. Published online 2023. doi:10.21203/rs.3.rs-2752706/v1

Water radiolysis reactions		
Chemical reactions	Reaction rates $(\mathbf{L.mol^{-1}.s^{-1}})$	Corrected reaction rates $(\mathbf{L.mol^{-1}.s^{-1}})$
$\mathbf{H^{\bullet} + H^{\bullet} \rightarrow H_2}$	$0.5\ 10^{10}$	
$\mathbf{e_{aq}^{-} + H^{\bullet} + H_2O \rightarrow H_2 + HO^{-}}$	$2.5\ 10^{10}$	
$\mathbf{e_{aq}^{-} + e_{aq}^{-} + 2H_2O \rightarrow H_2 + 2HO^{-}}$	$0.636\ 10^{10}$	
$\mathbf{H_3O^{+} + HO^{-} \rightarrow 2H_2O}$	$1.13\ 10^{11}$	
$\mathbf{HO^{\bullet} + H^{\bullet} \rightarrow H_2O}$	$1.55\ 10^{10}$	
$\mathbf{HO^{\bullet} + HO^{\bullet} \rightarrow H_2O_2}$	$0.55\ 10^{10}$	
$\mathbf{e_{aq}^{-} + HO^{\bullet} \rightarrow HO^{-}}$	$2.95\ 10^{10}$	
$\mathbf{e_{aq}^{-} + H_2O_2 \rightarrow HO^{-} + HO^{\bullet}}$	$1.10\ 10^{10}$	
$\mathbf{e_{aq}^{-} + H_3O^{+} \rightarrow H^{\bullet} + H_2O}$	$2.11\ 10^{10}$	$1.12\ 10^{10}$
$\mathbf{H^{\bullet} + O^{-} \rightarrow HO^{-}}$	$2.00\ 10^{10}$	
$\mathbf{H_3O^{+} + O_3^{-} \rightarrow OH + O_2}$	$9.00\ 10^{10}$	$4.77\ 10^{10}$
$\mathbf{H^{\bullet} + HO_2^{\bullet} \rightarrow H_2O_2}$	$1.00\ 10^{10}$	
$\mathbf{H^{\bullet} + O_2^{-} \rightarrow HO_2^{-}}$	$1.00\ 10^{10}$	
$\mathbf{HO^{\bullet} + O_2^{-} \rightarrow O_2 + HO^{-}}$	$1.07\ 10^{10}$	
$\mathbf{e_{aq}^{-} + O_2^{-} \rightarrow H_2O_2 + HO^{-} + HO^{-}}$	$1.3\ 10^{10}$	$2.43\ 10^{10}$
$\mathbf{e_{aq}^{-} + HO_2^{-} \rightarrow O^{-} + HO^{-}}$	$3.51\ 10^{9}$	$6.61\ 10^{9}$
$\mathbf{e_{aq}^{-} + O^{-} \rightarrow HO^{-} + HO^{-}}$	$2.31\ 10^{10}$	$4.35\ 10^{10}$
$\mathbf{H_3O^{+} + O_2^{-} \rightarrow HO_2^{\bullet}}$	$4.78\ 10^{10}$	$2.53\ 10^{10}$
$\mathbf{H_3O^{+} + HO_2^{-} \rightarrow H_2O_2}$	$4.78\ 10^{10}$	$2.65\ 10^{10}$
$\mathbf{H_3O^{+} + O^{-} \rightarrow HO^{\bullet}}$	$4.78\ 10^{10}$	$2.53\ 10^{10}$
$\mathbf{e_{aq}^{-} + HO_2^{\bullet} \rightarrow HO_2^{-}}$	$1.29\ 10^{10}$	
$\mathbf{HO^{\bullet} + HO^{-} \rightarrow O^{-}}$	$1.27\ 10^{10}$	
$\mathbf{HO^{\bullet} + HO_2^{\bullet} \rightarrow O_2}$	$7.90\ 10^{9}$	
$\mathbf{HO^{\bullet} + HO_2^{-} \rightarrow HO_2^{\bullet} + HO^{-}}$	$8.32\ 10^{9}$	
$\mathbf{HO^{\bullet} + O^{-} \rightarrow HO_2^{-}}$	$1.00\ 10^{9}$	
$\mathbf{HO^{\bullet} + O_3^{-} \rightarrow O_2^{-} + HO_2^{\bullet}}$	$8.50\ 10^{9}$	
$\mathbf{HO^{-} + HO_2^{\bullet} \rightarrow O_2^{-}}$	$1.27\ 10^{10}$	
$\mathbf{H_2O_2 + HO^{-} \rightarrow HO_2^{-}}$	$1.3\ 10^{10}$	
$\mathbf{H_2O_2 + O^{-} \rightarrow HO_2^{\bullet} + HO^{-}}$	$5.55\ 10^{8}$	
$\mathbf{H_2 + O^{-} \rightarrow H^{\bullet} + HO^{-}}$	$1.21\ 10^{8}$	
$\mathbf{O_2^{-} + O^{-} \rightarrow O_2 + HO^{-} + HO^{-}}$	$6.0\ 10^{8}$	$1.13\ 10^{9}$
$\mathbf{HO_2^{-} + O^{-} \rightarrow O_2^{-} + HO^{-}}$	$3.5\ 10^{8}$	$6.59\ 10^{8}$
$\mathbf{O^{-} + O^{-} \rightarrow H_2O_2 + HO^{-} + HO^{-}}$	$1.0\ 10^{8}$	
$\mathbf{O^{-} + O_3^{-} \rightarrow O_2^{-} + O_2^{-}}$	$7.0\ 10^{8}$	
$\mathbf{H^{\bullet} + HO^{-} \rightarrow e_{aq}^{-}}$	$2.51\ 10^{7}$	
$\mathbf{H^{\bullet} + H_2O_2 \rightarrow HO^{\bullet}}$	$3.50\ 10^{7}$	
$\mathbf{HO^{\bullet} + H_2O_2 \rightarrow HO_2^{\bullet}}$	$2.88\ 10^{7}$	
$\mathbf{HO^{\bullet} + H_2 \rightarrow H^{\bullet}}$	$3.28\ 10^{7}$	
$\mathbf{HO_2^{\bullet} + HO_2^{\bullet} \rightarrow H_2O_2 + O_2}$	$9.80\ 10^{5}$	
$\mathbf{HO_2^{\bullet} + O_2^{-} \rightarrow HO_2^{-} + O_2^{+}}$	$9.70\ 10^{7}$	
$\mathbf{O_2^{-} + O_2^{-} \rightarrow H_2O_2 + O_2 + 2HO^{-}}$	$1.00\ 10^{2}$	
Oxygen scavenging reactions		
$\mathbf{e_{aq}^{-} + O_2 \rightarrow O_2^{-}}$	$2.3\ 10^{10}$	
$\mathbf{H^{\bullet} + O_2 \rightarrow HO_2^{\bullet}}$	$1.3\ 10^{10}$	

$O^- + O_2 \rightarrow O_3^-$	$3.7\ 10^9$	
Water scavenging reactions		
$O_3^- + H_2O \rightarrow O^- + O_2$	$2.66\ 10^3$	
$HO_2^{\bullet} + H_2O \rightarrow H_3O + O_2^-$	$7.58\ 10^5$	
$H^{\bullet} + H_2O \rightarrow e_{aq}^- + H_3O$	6.32	
$e_{aq}^- + H_2O \rightarrow H^{\bullet} + HO^{\bullet}$	$1.58\ 10^1$	
$O_2^- + H_2O \rightarrow HO_2^{\bullet} + HO^-$	0.15	
$HO_2^- + H_2O \rightarrow H_2O_2 + HO^-$	$1.36\ 10^6$	
$O^- + H_2O \rightarrow HO^{\bullet} + HO^-$	$1.8\ 10^6$	
$e_{aq}^- + H_3O^+ \rightarrow H^{\bullet} + H_2O$	$2.09\ 10^3$	
$O_2^- + H_3O^+ \rightarrow HO_2^{\bullet} + H_2O$	$4.78\ 10^{10}$	$2.53\ 10^{10}$
$HO^- + H_3O^+ \rightarrow 2H_2O$	$1.13\ 10^{11}$	
$HO_2^- + H_3O^+ \rightarrow H_2O_2 + H_2O$	$4.78\ 10^{10}$	
$O^- + H_3O^+ \rightarrow HO^{\bullet} + H_2O$	$9.56\ 10^{10}$	$2.53\ 10^{10}$
$O_3^- + H_3O^+ \rightarrow HO^{\bullet} + O_2 + H_2O$	$9.0\ 10^{10}$	$4.77\ 10^{10}$
$H_3O^+ + HO^- \rightarrow 2H_2O$	$1.13\ 10^{11}$	$6.26\ 10^{10}$
$H^{\bullet} + HO^- \rightarrow H_2O + e_{aq}^-$	$2.49\ 10^7$	
$HO^{\bullet} + HO^- \rightarrow O^- + H_2O$	$1.27\ 10^{10}$	
$H_2O_2 + HO^- \rightarrow HO_2^{\bullet -} + H_2O$	$1.27\ 10^{10}$	
$HO_2^{\bullet} + HO^- \rightarrow O_2^- + H_2O$	$1.27\ 10^{10}$	

1